

Observations of High Energy Cosmic-Ray Electrons from 30 GeV to 3 TeV with Emulsion Chambers

T.Kobayashi

*Department of Physics and Mathematics, Aoyama Gakuin University, Sagamihara
252-5258, Japan*

tadasik-112850@jasper.dti.ne.jp

Y.Komori

Kanagawa University of Human Services, Yokosuka 238-0013, Japan

komori-y@kuhs.ac.jp

K.Yoshida, K.Yanagisawa

*College of Systems Engineering and Science, Shibaura Institute of Technology, Saitama
337-8570, Japan*

yoshida@shibaura-it.ac.jp

J.Nishimura, T.Yamagami, Y.Saito

*The Institute of Space and Astronautical Science, Japan Aerospace Exploration Agency,
Sagamihara 229-8510, Japan*

nisimura@icrr.u-tokyo.ac.jp

N.Tateyama

Faculty of Engineering, Kanagawa University, Yokohama 221-8686, Japan

tateyama@n.kanagawa-u.ac.jp

T.Yuda

Institute for Cosmic Ray Research, University of Tokyo, Kashiwa 277-8582, Japan

yuda@icrr.u-tokyo.ac.jp

and

R.J.Wilkes

Department of Physics, University of Washington, Seattle, USA

wilkes@u.washington.edu

ABSTRACT

We have performed a series of cosmic-ray electron observations using the balloon-borne emulsion chambers since 1968. While we previously reported the results from subsets of the exposures, the final results of the total exposures up to 2001 are presented here. Our successive experiments have yielded the total exposure of $8.19 \text{ m}^2 \text{ sr day}$ at the altitudes of $4.0 - 9.4 \text{ g cm}^{-2}$. The performance of the emulsion chambers was examined by accelerator beam tests and Monte-Carlo simulations, and the on-board calibrations were carried out by using the flight data. In this work we present the cosmic-ray electron spectrum in the energy range from 30 GeV to 3 TeV at the top of the atmosphere, which is well represented by a power-law function with an index of -3.28 ± 0.10 . The observed data can be also interpreted in terms of diffusive propagation models. The evidence of cosmic-ray electrons up to 3 TeV suggests the existence of cosmic-ray electron sources at distances within $\sim 1 \text{ kpc}$ and times within $\sim 1 \times 10^5 \text{ yr}$ ago.

Subject headings: cosmic rays: electrons, origin — balloons — supernova remnants

1. Introduction

Electrons¹ in cosmic rays have unique features, complementary to the cosmic-ray nuclear components, because of their low mass and leptonic nature. High-energy electrons lose energy by synchrotron radiation in the Galactic magnetic field and inverse Compton scattering with the interstellar photons in the Galaxy. High-energy cosmic-ray electrons cannot propagate

¹ In this paper, the term "electrons" is used for the sum of particles regardless of charge. When we must identify the charge, we will use the terms "negative electrons" or "positrons".

far from the sources, because the electrons lose rapidly energy with an energy loss rate of the square of energy through these radiative processes. These processes during the propagations through the Galaxy without hadronic interactions simplify modeling of the propagation of electrons compared with other cosmic-ray components such as nucleons.

Evidence for non-thermal X-ray emission from supernova remnants (SNRs) indicate that high-energy electrons in the TeV region are accelerated in SNRs (Koyama et al. 1995, e.g.). These observations strongly suggest that cosmic-ray electrons are accelerated in SNRs, and that SNRs are the most likely primary sources of cosmic-ray electrons. Shen (1970) first pointed out that the electron spectrum in the TeV region depends on the age and distance of a few local sources. His proposed concept has been accepted in later calculations of cosmic-ray electrons (Kobayashi et al. 2004, and references therein). Kobayashi et al. (2004) suggest that the energy spectrum of cosmic-ray electrons have unique spectral structures in the TeV region due to the discrete effect of local sources. This means that we can identify cosmic-ray electron sources from the electron spectrum in the TeV region. In addition, it is discussed that some dark matter may produce negative electrons and positrons in the energy region of around 100 – 10 TeV via dark matter annihilations or decaying dark matter (Kamionkowski & Turner 1991; Cheng et al. 2002, e.g.). In particular, in the case of mono-energetic electrons from dark matter, although propagation through the Galaxy would broaden the line spectrum, the observed electron spectrum could still have distinctive features. Thus, the observations of high-energy electrons bring us unique information about sources and propagation of cosmic rays, and enable us to search for dark matter.

Although the cosmic-ray electrons have been observed with many kinds of detectors since 1960 (Earl 1961), most observations are limited below several 100 GeV (Daniel & Stephens 1965; Golden et al. 1984; Tang 1984; Grimani et al. 2002; Boezio et al. 2000; DuVernois et al. 2001; Torii et al. 2001; Aguilar et al. 2002). Among these observations, the first-time cosmic-ray electron observation with nuclear emulsions was achieved by Daniel & Stephens (1965). They indicated that nuclear emulsions are ideal for the detection of electrons among many background protons because of the excellent imaging capability with a high position resolution of 1 μm .

The reason for the difficulty of the electron observations is that the electron flux itself is very low and decreases with energy much more rapidly than that of protons because of the electro-magnetic energy loss. The electron energy spectra are represented by a power-law function with an index of -3.0 to -3.3 , which is steeper spectra than the proton spectra with a power-law index of -2.7 (Haino et al. 2004, and references therein). The flux of cosmic-ray electrons is ~ 1 % of the protons at 10 GeV, and decreases very rapidly with increasing energy to be ~ 0.1 % of the protons at 1 TeV (Yoshida et al. 2008, e.g.). Therefore, there are few

observations of the electrons in the TeV region, since we need a long duration exposure with a detector that has a large geometrical factor, enough thickness, and powerful background rejection powers.

Chang et al. (2008) performed ATIC-2 balloon experiment in Antarctica and reported the energy spectrum in the energy region from 20 GeV up to 3 TeV, whose instrument contains a deep, fully active, BGO calorimeter of 18 radiation lengths (r.l.). They indicated an excess of cosmic-ray electrons at energies of 300 – 800 GeV, compared to a general electron spectrum calculated with the GALPROP (Moskalenko & Strong 2010). They discussed that the excess may indicate a nearby source of energetic electrons such as the annihilated electrons from dark matter particles. On the other hand, from the independent data analysis of ATIC-2 + ATIC-4, Panov et al. (2011) reported the electron spectrum from 30 GeV to 1 TeV, and indicated that the electron spectrum in the region of the excess includes a fine structure with a number of narrow peaks.

Torii et al. (2008) also observed cosmic-ray electrons from 10 GeV to 800 GeV by a long duration balloon flight using Polar Patrol Balloon (PPB) in Antarctica. The PPB-BETS is an imaging calorimeter composed of scintillating-fiber belts and plastic scintillators inserted between lead plates with 9 r.l. They discussed that the energy spectrum with PPB-BETS may indicate a sign of a structure in the several 100 GeV region, which is similar with the ATIC-2 observations, although a single power-law spectrum is acceptable within statistical errors.

Ackermann et al. (2010b) presented the results of cosmic-ray electron observations from 7 GeV to 1 TeV using about 8×10^6 electron candidates detected in the first 12 months on-orbit by the Fermi Large Area Telescope (Fermi-LAT). Their electron spectrum can be described with a power law of $\propto E^{-3.08 \pm 0.05}$ with no prominent features, accommodating a slight spectral hardening at around 100 GeV and a slight softening above 500 GeV. Fermi-LAT also searched for anisotropies of electrons from 60 GeV to 480 GeV with angular scale extending from $\sim 10^\circ$ to 90° , resulting in nul results (Ackermann et al. 2010a). They indicated that the upper limits for a dipole anisotropy range from $\sim 0.5\%$ to $\sim 10\%$. Although the Fermi-LAT has the large exposures of the electron observations, the detector thickness is insufficient to observe electrons in the TeV region. As the result, Fermi-LAT cannot separate electrons and protons one by one, but separated electrons from protons statistically based on Monte-Carlo simulations and machine learning algorithms.

The H.E.S.S. ground-based imaging atmospheric Cherenkov telescopes measured the electron spectrum in the energy range of 340 GeV to 5 TeV (Aharonian et al. 2008, 2009). The H.E.S.S. data show no indication of a structure in the electron spectrum, but rather a power-law spectrum with a spectral index of -3.0 which steepens to be around -4.0 above

~ 1 TeV. While H.E.S.S. team reported electron observations up to several TeV, the electron spectrum is provided by indirect observations. Thus, H.E.S.S. intrinsically has systematic errors on the reconstructed electron spectra arising from uncertainties in the simulation of hadronic interactions, the atmospheric model, and the absolute energy scale.

Adriani et al. (2009) reported a statistically significant increase in the positron fraction at energies above ~ 10 GeV with the PAMELA satellite-borne experiment, which is completely inconsistent with standard models describing the secondary production of cosmic rays. The PAMELA positron data indicate the existence of primary positron sources such as the annihilation of dark matter particles in vicinity of our Galaxy, nearby pulsars, and nearby micro-quasars. Adriani et al. (2011a) also presented the negatively charged cosmic-ray electron spectrum between 1 and 625 GeV performed by PAMELA, which is the first time that cosmic-ray negative electrons have been identified separately from positrons above 50 GeV. The negative electron spectrum can be described with a single power law energy dependence with a spectral index of -3.18 ± 0.05 above 30 GeV and no significant spectral features.

We have observed high-energy cosmic-ray electrons from 30 GeV to 3 TeV with emulsion chambers at balloon altitudes, from 1968 to 2001, accumulating a total exposure of $8.19 \text{ m}^2 \cdot \text{sr} \cdot \text{day}$. In the observations, we have carried out particle identification one event by one event with a proton rejection power larger than 1×10^5 in TeV region, because of an excellent imaging detector with a position resolution of $1 \mu\text{m}$, which is one of the outstanding capabilities of the emulsion chambers. The performance of the emulsion chambers was examined with accelerator beam tests at CERN-SPS and Monte-Carlo simulations. We also estimated the atmospheric electron spectra in a reliable way (Komori et al. 2012), and carried out on-board calibrations by using the flight data.

While we previously reported the results from 1968 to 1976 experiments (Nishimura et al. 1980) and some additional publications (see references of Kobayashi et al. (2004)), in this paper we present the final cosmic-ray electron spectrum in the energy range from 30 GeV to 3 TeV observed with the balloon-borne emulsion chambers up to 2001, combined with our previous results.

2. Detector

Emulsion chambers consists of nuclear emulsion plates, X-ray films, and lead plates (or tungsten plates in a few chambers). A nuclear emulsion plate is a methacrylate base $500 - 800 \mu\text{m}$ thick, double coating of nuclear emulsion with $50 - 100 \mu\text{m}$ thickness. We

used Fuji ET-7B and ET-7D for nuclear emulsion. Nuclear emulsion plates are placed under lead plates. One or two X-ray films are inserted between a lead plate and a nuclear emulsion plate to allow rapid, naked-eye scanning for high-energy cascade showers, which produce dark spots in the films. Figure 1 shows a typical emulsion chamber configuration. The typical size and thickness of the detector are $40\text{ cm} \times 50\text{ cm}$ and 8 cm ($\sim 9\text{ r.l.}$), respectively. Detailed configurations are described in Nishimura et al. (1980).

The thickness of one lead plate at the upper layers is 0.5 mm ($\sim 0.09\text{ r.l.}$) to identify incident parent particles, determine the incident angles, and investigate the initial shower developments. At the bottom layers, the thickness of one lead plate is 5 mm ($\sim 0.9\text{ r.l.}$) and X-ray films are inserted to detect cascade showers, as shown in Fig. 1.

Since high-energy electro-magnetic showers above a few 100 GeV leave dark spots on X-ray films, these showers can be detected with the naked eye by scanning the X-ray films. The corresponding tracks in the adjacent emulsion plate are located by using microscopes. The detection threshold of the X-ray film is 500 GeV for Sakura type-N X-ray film used before 1984, 750 GeV for Fuji #200 X-ray film, and 250 GeV , 200 GeV , 150 GeV for screen type X-ray films of Fuji G8-RXO, G12-RXO, and GS-RXO used from 1984 to 1988 (Kobayashi et al. 1991). After 1988 we used screen type X-ray films of HR8-HA30, HR12-HA30, and HR16-HA30. The sensitivity experiment of screen type X-ray films of HR series were carried out at Research Center for Electron Photon Science of Tohoku University in 2001 using test chambers with multilayers of emulsion plates and X-ray films. The test chambers were exposed to the 200 MeV electron beams. Figure 2 shows the result of the characteristic curves of different type of X-ray films. Since the detection threshold of the net darkness on the X-ray films with naked eye is 0.1 (Kobayashi et al. 1991), the electron densities on the emulsion plates at the X-ray film detection threshold correspond to $0.9 \times 10^5\text{ cm}^{-2}$ for HR16-HA30, $1.2 \times 10^5\text{ cm}^{-2}$ for HR12-HA30, $2.6 \times 10^5\text{ cm}^{-2}$ for HR8-HA30, and $4.0 \times 10^5\text{ cm}^{-2}$ for Fuji #200 X-ray films. These electron densities are compatible with the shower track densities with emulsion chambers at the shower maximum of electrons with energies of 140 GeV , 180 GeV , 450 GeV , and 750 GeV , respectively (see Fig. 6), which are the detection threshold energies of the X-ray films.

Figure 1

Figure 2

Because of the simple configuration of the detector, the geometrical factor ($S\Omega$) can be estimated very accurately, a difficult task for some electronic detectors. For the electron observations, the effective geometrical factor is given by

$$S\Omega_e = 2\pi S\eta \int_0^{\theta_0} \cos\theta \sin\theta d\theta = \pi S\eta \sin^2\theta_0, \quad (1)$$

where θ_0 is the upper limit of incident angles and η is so-called "edge effect". Since the detector has its edge, some incident electrons near the edge on the top of the detector do not pass through the bottom of the detector. The edge effect is the efficiency of events that pass through the top and bottom emulsion plates. In the typical case of $\theta_0 = 60^\circ$ and $S = 0.40 \times 0.50 \text{ m}^2$, $S\Omega_e$ is $0.39 \text{ m}^2 \text{ sr}$ with η of 0.82 for the chamber thickness of 8.0 cm. In appendix A, we summarize the area S , edge effect η , upper limit of incident angles θ_0 , and $S\Omega_e T$ of the emulsion chambers. As shown in appendix A, S , η , θ_0 , and $S\Omega_e T$ change depending on the electron energies.

We measure the shower particles within a circle of $100 \mu\text{m}$ radius from shower axis. This means that we select the shower particles with higher energies, which suffered less multiple scattering in the chamber. Hence, the number of the shower particles selected decreases faster than that of all shower particles. The shower maximum in emulsion chambers for the shower particles within a circle of $100 \mu\text{m}$ radius appears in ~ 6 r.l. for 1 TeV electrons, while the maximum of the total number of shower particles appears in ~ 12 r.l. for 1 TeV electrons. As a result, the energy of higher energy incident electrons can be determined with a thinner detector. Thus the emulsion chamber has the advantages of a wide field of view, small thickness, and lightweight detector, compared to the other instruments.

In order to verify the zenith angle dependence of the detection efficiency for the incident electrons, we present the zenith angle distribution of electrons observed with the balloon-borne emulsion chambers in Fig. 3, which is compared to the expected distribution for primary cosmic-ray electrons. As shown in Fig. 3, the zenith angle distribution of electrons is consistent with the expectation.

Figure 3

3. Balloon observations

We have observed cosmic-ray electrons with balloon-borne emulsion chambers in 14 flights between 1968 and 2001. In order to reject background cosmic rays, the emulsion

chambers are placed upside down in the balloon gondolas during ascent and descent of the balloons, and are flipped to a normal position during level flight. The pressure altitude records for each flight correspond to residual atmospheric overburdens in the range from 4.0 g cm^{-2} to 9.4 g cm^{-2} . In Table 1, we summarize the series of experiments since 1968, in which the results for 1968 – 1976 observations were reported in Nishimura et al. (1980). The $S\Omega_e T$ in Table 1 present the effective exposure factors for primary electron observations in the energy range above 1 TeV within the zenith angle of 60° . Figure 4 shows the total cumulative effective exposure $S\Omega_e T$ for primary electrons, which is $8.19 \text{ m}^2\text{-sr-day}$ in the TeV region. In addition to the electron observations, we have simultaneously observed atmospheric gamma rays, whose results are described in Yoshida et al. (2006).

Table 1

Figure 4

4. Data Analysis

In the balloon observations, we identify electron events among incoming cosmic-ray events and determine the energies. In the following data analysis, we selected events with incident zenith angle less than 60 degree and which passed all the way from the top to bottom layer of the chambers.

4.1. Event identification

High-energy electro-magnetic showers above a few 100 GeV are detected with naked-eye scanning of dark spots left on the X-ray films. The corresponding tracks in the adjacent emulsion plate are located with microscopes, and traced back through the stack to the shower starting points. As described in section 2 and appendix A, since we have improved the X-ray films to detect lower energy electrons, we have used different types of X-ray films that have the different threshold energies. Hence, the total cumulative effective exposure $S\Omega_e T$ depends on electron energies, as shown in Fig. 4. The detection efficiencies are 100 % above the threshold energies and fall off rather rapidly below the thresholds (Nishimura et al. 1980).

We also confirmed the threshold energy for each balloon flight by using the deviation from a single power-law spectrum of the observed atmospheric gamma rays. In this analysis, we used the electron events above the threshold energies to derive the electron energy spectrum. In order to detect the electro-magnetic showers below a few 100 GeV, the emulsion plates were directly scanned with microscopes for a part of the 1968, 1969, 1970, 1973, and 1996 emulsion chambers. We successfully detected electron events down to 30 GeV with the microscope scanning. The detection efficiency is larger than 95% (Nishimura et al. 1980). The microscope scanning is carried out in the smaller rectangular area of the upper emulsion plates. Since the shower particles on the bottom emulsion plates are measured in the full area, the edge effect η of the microscope scanning has the larger value than that of the usual shower measurements. In the case of the scanning area within $d\tan\theta_0$ from the detector edge, where d is the thickness of the detector and θ_0 is the upper limit of incident angles, η is 1.00. For the larger scanning area, not within $d\tan\theta_0$ from the detector edge, η is smaller than 1.00, as shown in Table A1. In emulsion chambers, it is possible to measure the location of shower tracks in each emulsion plate with a precision of 1 μm . The incoming particles such as electrons, gamma-rays, protons, and heavier nuclei are identified by examining the details of shower development, especially around the shower starting points.

Since electron events start from a single charged track which produces an electron-positron pair within 1 r.l. of the top of the emulsion chamber with about 90 % probability, they are identified by the existence of a single and a pair track with the spreading angle less than 1×10^{-3} rad at the interaction point, as described in Appendix B. Electron events also give the electro-magnetic shower without core structures. Gamma-ray events, which are also a pure electro-magnetic shower, start from a pair with no visible primary track above the shower starting point. Although the incident track of a proton-induced shower shows a single charged track like an electron, proton-induced showers also have many secondaries at the shower starting point and often have multi core structures in the deep layers. Even in the case of proton-induced showers with few secondary tracks, it is possible to discriminate the proton-induced showers from electron-induced showers by the differences of the spreading angle between tracks at the shower starting points. As described in Appendix B, the proton rejection power is estimated to be larger than 1×10^5 , that is derived to be independent of M.C. simulation codes and hadron interaction models. Hadron showers of heavier nuclei such as helium are easily distinguished because the grain density of the incident track is larger than a minimum ionizing particle.

In emulsion chambers, we can measure the depth of the first electron-positron pair of the electron-induced shower, the so called shower starting point. The validity of event identification can be checked by comparison of the measured shower starting points with the expected values. Figure 5 presents the shower starting point distributions of the bal-

loon observations for electrons above 400 GeV, gamma rays above 300 GeV, and protons, compared to the expected distributions. As for the electrons, the shower starting point is compared to the Bethe-Heitler expectation and the LPM expectation based on Migdal’s formula (Baier & Katkov 2005, e.g.). As shown in Fig. 5, the shower starting point distributions within 3.0 r.l. show good agreement with the expectations, whose results suggest the reliability of the particle identification, and the deviation of the proton distribution larger than 3.0 r.l. from the expectation shows the decrease of the proton detection efficiency. In particular, the consistent result of the electrons with the LPM expectation strongly suggests the accurate identification of electrons.

Figure 5

4.2. Energy Determination

Electron energies were determined by counting the number of shower tracks in each emulsion plate within a circle of radius $100\mu\text{m}$ centered on the shower axis. We derived the integral track length from these counted tracks in each layer. The integral track length is theoretically expected to be proportional to the shower energy, as discussed in detail in Nishimura et al. (1980). Our chamber structures are slightly different in each flight because of slight differences of lead thicknesses and insertion of different types of X-ray films and phosphoric screen films. Since the differences of the chamber structure affect the integral track lengths, we calculated the shower developments for each chamber one by one using a Monte-Carlo simulation code called Epics (Kasahara 2012). Epics has been used for cosmic-ray experiments (Torii et al. 2001; Amenomori et al. 2009, e.g.), and also used for very forward single photon energy spectra from 0.1 TeV to 3.6 TeV in the Large Hadron Collider forward (LHCf) experiments (Adriani et al. 2011b). The incident electron energies are determined by these track lengths compared with the values estimated from the Monte-Carlo simulations for each chamber.

For the calibration of the detector, we carried out beam tests of electrons in 2004 at CERN-SPS. The detector configuration is same as the balloon-borne emulsion chambers, except for the detector size of $10.0\text{ cm} \times 12.5\text{ cm}$. Results calculated using the Epics code were confirmed by emulsion chambers exposed to 50 GeV and 200 GeV electron beams at CERN-SPS. In order to evaluate the possible systematic errors at energies greater than 200 GeV, we also compared two independent Monte-Carlo simulation codes; Epics and Geant4 (Agostinelli et al. 2003; Amako et al. 2006). Figure 6 shows the longitudinal devel-

opment of the average number of shower tracks from the Monte-Carlo simulations, compared with the results of 50 GeV and 200 GeV electron beams. As shown in Fig. 6, the simulations well represent the experimental data. The differences between the integral track lengths of Epics and Geant4 are $\sim 2\%$ in the energy range of 30 GeV – 3 TeV, which is negligible small compared to statistical errors of our cosmic-ray electron spectrum as described in section 4.3. Figure 7 shows the energy distributions for 50 GeV and 200 GeV electron beams. The determined energies with the simulations for 50 GeV and 200 GeV electrons are consistent with the experimental data. The energy resolutions are 14.5 % at 50 GeV and 10.6 % at 200 GeV, respectively. Figure 8 presents the energy resolutions of the simulations, compared with the experimental data. The energy resolution for the emulsion chamber is well represented by the form of

$$\frac{\sigma}{E} = [8.6\%^2(\frac{E}{100\text{GeV}})^{-1} + 6.9\%^2 + 2.4\%^2(\frac{E}{100\text{GeV}})]^{1/2}, \quad (2)$$

where E is the electron energy and σ is the standard deviation of energy determination. The first term in right-hand side root represents statistics-related fluctuations of the number of shower particles, while the last term represents fluctuations due to shower particles escaping from the finite thickness of the detector.

Figure 6

Figure 7

Figure 8

4.3. Electron energy spectrum

In balloon flight experiments, it is necessary to correct the observed cosmic-ray electron spectrum because of the residual overlying atmosphere. We corrected energy loss of primary electrons due to bremsstrahlung radiation in the overlying atmosphere. The average bremsstrahlung energy loss to each electron is given by

$$E_0 = E e^{\frac{A(s)}{s} \cdot \frac{t}{\cos\theta}}, \quad (3)$$

when the incident electron spectrum is a power-law function with an index of $-(s+1)$. Here, E_0 is the energy of primary electron at the top of atmosphere, E is the measured energy in the detector, t is the vertical thickness of the overlying atmosphere in radiation lengths, θ is a zenith angle of the incident electron to the detector, and $A(s)$ refers to the function used in electro-magnetic shower theory ², described by Nishimura (1967). In the case of $s = 2.3$, $A(2.3)$ is 1.674. For example, in the case of a power-law index of -3.3 ($s = 2.3$), an atmospheric thickness of 6.0 g cm^{-2} , and a zenith angle of 45 degree, the energies of incident electrons are reduced by 16 %, and hence the electron flux decreases by 32 %. This energy loss formula is different from the simple energy loss of $E_0 = Ee^{t/\cos\theta}$, since the energy losses of electrons have broad distributions and the incident electron spectrum is steeply sloped. In the case of $E_0 = Ee^{t/\cos\theta}$ with the same parameters, the energies are reduced by 21 % and the electron flux decreases by 41 %, which correspond to monochromatic electrons.

In addition to primary cosmic-ray electrons, atmospheric electrons are also produced by hadronic interactions of primary cosmic rays with nuclei in the atmosphere. Since almost all atmospheric electrons are produced via atmospheric gamma rays from neutral pion decay, the atmospheric electron spectrum is estimated by using the simultaneously observed atmospheric gamma-ray spectrum with the emulsion chambers (Yoshida et al. 2006). Komori et al. (2012) derived the atmospheric electron spectrum in the upper atmosphere less than 10 g cm^{-2} from the observed gamma-ray spectrum using the electro-magnetic shower theory. Their derived atmospheric electron spectrum is substantively free from the uncertainties of the cosmic-ray nuclear spectra and hadronic interaction models. The contributions of the atmospheric electrons to primary electrons increase with electron energies and with thicknesses of the overlying atmosphere. Table 2 shows the number of atmospheric electrons, which ranges from 0 % to 50 % of the observed electrons.

We observed electrons at each balloon altitude, and derived the cosmic-ray electron spectrum using the following formula:

$$J_e(E) = \frac{N_e - N_{2\text{nd}}}{S\Omega_e T \Delta E C_{\text{eff}} C_{\text{enh}}} (\text{m}^{-2}\text{s}^{-1}\text{sr}^{-1}\text{GeV}^{-1}). \quad (4)$$

Here, N_e is the number of the observed electron events, $N_{2\text{nd}}$ is the number of atmospheric electrons, C_{eff} is electron detection efficiency, C_{enh} is enhancement factor due to the energy resolution.

² $A(s)$ is given by as follows:

$$A(s) = 1.36 \frac{d\log\Gamma(s+2)}{ds} - \frac{1}{(s+1)(s+2)} - 0.075.$$

The efficiency C_{eff} for detecting electro-magnetic showers in emulsion chambers have been studied to be essentially 100 % above the threshold energy for naked-eye scanning of X-ray films (Kobayashi et al. 1991, and references therein). The detection efficiency for HR16-HA30 was also tested by using emulsion chambers exposed to the 200 GeV electron beam at CERN-SPS. Simultaneously with primary electrons, we have also observed atmospheric gamma rays to check the performance of the emulsion chambers in each balloon experiment (Yoshida et al. 2006). We also confirmed the detection efficiency of each emulsion chamber from the atmospheric gamma-ray spectra. The uncertainty of the energy determination has the effect of enhancing the absolute flux of electrons, in particular, for a steep power-law spectrum. The enhancement factor C_{enh} due to the energy resolution has values from 1.01 to 1.09, depending on electron energies (see Yoshida et al. (2006) in detail).

5. Results and discussions

The total number of the observed electrons is 166 events with the balloon-borne emulsion chambers exposed from 1968 to 2001 in the energy range of 30 GeV to 3 TeV. After the corrections described above, we derived the primary cosmic-ray electron energy spectrum. Figure 9 shows the observed electron spectrum, which is well represented by a power-law function of

$$J_e(E) = (1.39 \pm 0.23) \times 10^{-4} (E/100 \text{ GeV})^{-3.28 \pm 0.10} (\text{m}^{-2} \text{s}^{-1} \text{sr}^{-1} \text{GeV}^{-1}). \quad (5)$$

The flux values and numbers of the electrons in each energy bin are listed in Table 2. Compared with our previous electron spectrum in the energy range of 30 – 1000 GeV (Nishimura et al. 1980), the total number of the observed electrons increased threefold the previous result, and the highest energy was extended up to 3 TeV.

Figure 9

Table 2

The cosmic-ray electrons observed with balloon-borne emulsion chambers (ECC) extend up to 3 TeV with no cut off in the form of a power-law spectrum with an index of -3.28 . In

order to confirm the lower limit of high-energy cut off in TeV region, we fitted the observed electron spectrum with an exponentially cut-off power law. With the fixed power-law index of -3.28 , the lower limit (90 % C.L.) of the exponential cut-off energy is 2.1 TeV.

This observed electron spectrum in the energy region below 1 TeV is very similar to the electron spectrum by PAMELA (Adriani et al. 2011a), and shows agreement with the electron observations by Fermi-LAT (Ackermann et al. 2010b). Our electron spectrum observed with the emulsion chambers does not exhibit significant spectral excesses. The result of our electron spectrum compared with the ATIC electron spectrum (Chang et al. 2008) is inconsistent, with a statistical significance level of 5 % (a reduced χ^2 value of 1.834 for d.o.f.= 11), although it is acceptable with a statistical significance level of 1 %. Above 1 TeV region, the comparison of our result with the electron spectra by H.E.S.S. is consistent, with a reduced χ^2 value of 1.121 for d.o.f.= 7, while H.E.S.S. data have large systematic errors (Aharonian et al. 2008, 2009).

We calculated an electron spectrum by GALPROP code using a standard file, galdef_50p_599278 (Moskalenko & Strong 2010). As shown in Fig. 10, this spectrum is consistent with the electron spectrum observed with the emulsion chambers. We also compared the observed electron energy spectrum with an electron spectrum calculated by Kobayashi et al. (2004), in which parameters are set as follows: the diffusion coefficient of $D_0 = 2.0 \times 10^{29} \text{ cm}^2 \text{ s}^{-1}$ at 1 TeV, the supernova rate of $1/40 \text{ yr}^{-1}$ in the Galaxy, the electron output energy of $1 \times 10^{48} \text{ erg}$ above 1 GeV, the 20 TeV cutoff energy of the electron injection spectrum, and the burst-like release at $\tau = 5 \times 10^3 \text{ yr}$ after the explosion. The "distant component" in Fig. 10 indicates the contributions from continuously distributed distant SNRs with the distance larger than 1 kpc or the age older than $1 \times 10^5 \text{ yr}$. As shown in Fig. 10, our observed spectrum is consistent with the calculated spectra of the distant component + nearby component by Kobayashi et al. (2004), giving strong evidence for a non-zero flux in the TeV region, by the definite identification of electron events one by one. Figure 10 also presents that the electron energy spectrum observed with emulsion chambers has the significantly larger flux in the TeV region than that of the distant component. This suggests that nearby electron sources such as SNRs exist within the distance of 1 kpc and the age of $1 \times 10^5 \text{ yr}$.

Figure 10

6. Conclusions

We have carried out cosmic-ray electron observations with the balloon-borne emulsion chambers since 1968. The emulsion chamber is an excellent imaging detector with a high position resolution of $1\ \mu\text{m}$. This imaging capability enables the emulsion chamber to identify electrons with the high rejection power against gamma rays and protons, which is the highest proton rejection power of 1×10^5 among the existing cosmic-ray electron detectors, and to determine electron energies by using only the central part of the electro-magnetic shower. This leads for the emulsion chamber to have thin thickness, lower mass, and a wide field of view, compared to the other detectors. Hence, the emulsion chambers, even the comparatively lightweight instruments, successfully observed electrons above several 100 GeV in the late 1960s and electrons above 1 TeV in the 1980s. Further, these electron observations initiated discussions about the investigation of the propagation mechanisms in the Galaxy and the identification of nearby cosmic-ray electron sources. Being recognized for the significance of the electron observations, the high-energy electron observations opened up and have been recently carried out by ATIC, Fermi-LAT, H.E.S.S., PAMELA, and so on. In order to identify nearby cosmic-ray electron sources and search for dark matter signals, there are also some ongoing and new experiments for the high-energy electron observations such as AMS-02 and CALET on the International Space Station (ISS) (Battiston et al. 2008; Torii et al. 2011). AMS-02 is ongoing to observe positrons and negative electrons up to 1 TeV. CALET is being developed to be installed on the ISS, preserving the excellent imaging characteristics of the emulsion chamber.

We sincerely thank the late Prof. J.J.Lord and the late Prof. T.Taira, who started up this experiment program, brought us to many successful balloon observations, and worked on the development of the experiments. We are also grateful to a number of collaborators who have carried out together the experiments since 1968. We thank the crews of the Sanriku Balloon Center (SBC) of ISAS/JAXA and the NASA Columbia Scientific Balloon Facility (CSBF) for their excellent and successful balloon flights. We acknowledge the staffs of Institute for Cosmic Ray Research (ICRR), University of Tokyo for their kind support to emulsion experiments. We also appreciate the excellent work and kind support of the staffs in Research Center for Electron Photon Science of Tohoku University and the H4 beam line of CERN-SPS. We are grateful to Y. Sato for his kind support at CERN in the beam tests.

A. A list of emulsion chambers

Table A1

B. Proton rejection power

The flux of cosmic-ray electrons is much smaller than that of cosmic-ray protons. The observed flux ratio of electrons against protons is around 1 % for 10 GeV and 0.1 % for 1 TeV. Therefore, in order to observe high-energy electrons above 1 TeV, the proton rejection power is required to be at least larger than 1×10^4 . We estimate the proton rejection power with the emulsion chamber in the following.

B.1. Mean free path for hadronic interactions

While an electron produces the first e^-e^+ pair within 2 r.l. with the probabilities of 99.9 % for 100 GeV electrons and 99.5 % for 1 TeV electrons with the threshold energy of 10 MeV for pair production, a proton interacts hadronically with a mean free path (m.f.p.) of about 30 r.l. in lead. Hence, the probability for hadronic interactions of a proton within 2 r.l. in the emulsion chamber is $2/30$, so that the proton rejection power for the difference between interaction lengths of electrons and protons is about 15.

B.2. Energy shift of proton-induced shower

Secondary neutral pions produced via hadronic interactions of a proton have in total about 30 % of the parent proton energy. Therefore, giving the same shower energy with an electron, the energy of the parent proton should be three times larger than that of the electron. Since the integral cosmic-ray proton spectrum has a power-law form of $E^{-1.7}$, the effective flux of protons is reduced to be $0.3^{1.7} \simeq 1/7$. Thus, the proton rejection power for the energy shift effect of the proton-induced shower is about 7.

B.3. Shower starting point

Electrons produce gamma rays via bremsstrahlung radiation, and then the gamma rays produce e^-e^+ pairs. Therefore, the almost electron-induced shower at the starting point in the emulsion chamber is composed of 3 tracks (one electron + one e^-e^+ pair) or 5 tracks (one electron + two e^-e^+ pairs). The mean spreading distance r of a parent electron and an e^-e^+ pair by Coulomb scattering is approximately given by

$$r \simeq \frac{1}{\sqrt{3}} \frac{E_s}{E} \left(\frac{x}{X_0} \right)^{1/2} L, \quad (\text{B1})$$

where x is a traversing thickness of the electron in the material, X_0 is a radiation length of the material, L is a path length of the electron, E is the electron energy, and E_s is the scattering constant of ~ 20 MeV. In the case of $x = X_0$ (i.e. 0.56 cm for lead) and $L = 1$ cm, the spreading distance r is $2 \mu\text{m}$ for the primary electron energy of 100 GeV and $0.2 \mu\text{m}$ for that of 1 TeV, taking the electron energy E to be a half of the incident electron energy because of the energy loss by bremsstrahlung radiation.

Among hadronic interactions of high-energy protons with nuclei, possible candidates to be the mimic electron events of protons are the following events. The forward produced charged secondary particles are narrowly collimated without the heavily ionizing tracks, which are recorded by low-energy recoil protons and nuclei, and the number of the charged secondary particles is just 1, 3 or 5, accompanied with one neutral pion. In addition, they have no multi-structures in their cascade showers. In fact, there are such phenomena that the momentum transfer to the target nuclei is relatively low and hence the number of the secondary particles is relatively small, what is called diffraction dissociation.

In order to study diffractive coherent production in hadronic interactions of protons with nuclei, the experiments with nuclear emulsions have been performed for 400 GeV and 800 GeV of proton beams by Boos et al. (1978) and Abduzhamilov et al. (1988), respectively. They selected the events with the number of the secondary charged particles of 1, 3 or 5, with the relatively low momentum transfer to the target nuclei, and without the heavily ionizing tracks. According to their results, the fractions of these selected events to the total hadronic interaction events are 3 % for 400 GeV protons and 2 % for 800 GeV protons.

Given that the spreading angle of the forward produced secondary particles is 1×10^{-3} rad, the radial distance between the secondary particles is $10 \mu\text{m}$ with a path length of 1 cm. Since this distance is one order of magnitude larger than the typical distance between a parent electron and an electron-positron pair, the proton events with the spreading angle larger than 1×10^{-3} rad are readily identifiable from the electron events. Adding the condition of the spreading angles less than 1×10^{-3} rad, the residual events are less than 4 % of the

measured diffraction dissociation events, that is, the fraction of the selected events to the total hadronic interaction events is less than $3\% \times 4\% = 0.12\%$ for 400 GeV protons and $2\% \times 4\% = 0.08\%$ for 800 GeV protons.

For the electron-like events of protons, since there are also further conditions that the selected events should be accompanied with one neutral pion and have no multi-structures in the shower developments, the above fraction gives us just the upper limit. Hence, the proton rejection power with the shower starting point is estimated to be larger than $1/0.1\% = 1 \times 10^3$.

B.4. Total proton rejection power

As described above, the proton rejection powers are 15 for the difference between interaction lengths of electrons and protons, 7 for the energy shift effect of the proton-induced shower, and $> 1 \times 10^3$ for the shower starting point, respectively. Combined these independent proton rejection powers, the total proton rejection power is estimated to be larger than $15 \times 7 \times (1 \times 10^3) = 1 \times 10^5$. Thus, for the electron observations with the emulsion chambers, the proton contamination in the TeV region is estimated to be less than $\sim 1\%$.

REFERENCES

- Adbo, A.A. et al. (Fermi-LAT Collaboration), 2009, Phys. Rev. Lett. 102, 181101
- Abduzhamilov, A. et al. 1988, Mod. Phys. Lett. A 3, 489
- Ackermann, M. et al. (Fermi-LAT Collaboration), 2010, Phys. Rev. D, 82, 092003
- Ackermann, M. et al. (Fermi-LAT Collaboration), 2010, Phys. Rev. D, 82, 092004
- Adriani, O. et al. 2009, Nature, 458, 607
- Adriani, O. et al. 2011a, Phys. Rev. Lett., 106, 201101
- Adriani, O. et al. 2011b, Phys. Lett. B, 703, 128
- Agostinelli, S. et al. 2003, Nucl. Instrum. Methods Phys. Res. A, 506, 250
- Amako, K. et al. 2006, IEEE Trans. Nucl. Sci., 53, 270
- Aharonian, F. et al. (H.E.S.S. Collaboration), 2008, Phys. Rev. Lett., 101, 261104

- Aharonian, F. et al. (H.E.S.S. Collaboration), 2009, *A&A*, 508, 561
- Aguilar, M. et al. 2002, *Physics Reports*, 366, 331
- Amenomori, M. et al. 2009, *ApJ*, 692, 61
- Baier, V.N., & Katkov, V.M., 2005, *Phys. Rep.*, 409, 261
- Battiston, R. on behalf of the AMS-02 collaboration, 2008, *Nucl. Instr. Meth. A*, 588, 227
- Beatty, J.J. et al. 2004, *Phys. Rev. Lett.*, 93, 241102
- Boezio, M. et al. 2000, *ApJ*, 532, 653
- Boos, E.G. et al. 1978, *Nucl. Phys. B*, 137, 37
- Chang, J. et al., 2008, *Nature*, 456, 362
- Cheng, H.C., Feng, J.L., & Matchev, K.T. 2002, *Phys. Rev. Lett.*, 89, 211301
- Daniel, R.R., & Stephens, S.A. 1965, *Phys. Rev. Lett.*, 15, 769
- DuVernois, M.A. et al. 2001, *ApJ*, 559, 296
- Earl, J.A., 1961, *Phys. Rev. Lett.*, 6, 125
- Golden, R.L. et al. 1984, *ApJ*, 287, 622
- Grimani, C. et al. 2002, *A&A*, 392, 287
- Haino, S. et al. 2004, *Phys. Lett. B*, 594, 35
- Kamionkowski, M. & Turner, M.S., 1991, *Phys. Rev. D*, 43, 1774
- Kasahara, K., 2012, <http://cosmos.n.kanagawa-u.ac.jp/>
- Kobayashi, T. et al. 1991, *Nuovo Ciment A*, 104, 1753
- Kobayashi, T., Komori, Y., Yoshida, K. & Nishimura, J., 2004, *ApJ*, **601**, 340.
- Komori, Y., Kobayashi, T., Yoshida, K. & Nishimura, J., 2012, *Astropart. Phys.*, in press
(<http://dx.doi.org/10.1016/j.astropartphys.2012.08.003>)
- Koyama, K. et al. 1995, *Nature*, 378, 255
- Moskalenko, I.V. & Strong, A.W., 2010, <http://galprop.stanford.edu/>

Nishimura,J., 1967, Handbuch der Physik, 46, II, 1, Springer

Nishimura,J. et al. 1980, ApJ, 238, 394

Panov,A.D. et al. 2011, Astrophys. Space Sci. Trans., 7, 119

Shen,C.S., 1970, ApJ, 162, L181

Tang,K.K., 1984, ApJ, 278, 881

Torii,S. et al. 2001, ApJ, 559, 973

Torii,S. et al. 2008, arXiv:0809.0760v1 [astro-ph]

Torii,S. on behalf of the CALET collaboration, 2011, Nucl. Instr. Meth. A, 630, 55

Yoshida,K., Ohmori,R., Kobayashi,T., Komori,Y., Sato,Y., and Nishimura,J., 2006, Phys. Rev. D, 74, 083511

Yoshida,K., 2008, Adv. Space Res., 42, 477

Table 1: List of balloon flights

Flight	Area (m ²)	Time (min)	Average Altitude (g cm ⁻²)	$S\Omega_e T$ * (m ² sr s)	Launch Site
1968	0.05	380	6.1	1.826×10^3	Harunomachi, Japan
1969	0.05	267	7.1	1.283×10^3	Harunomachi, Japan
1970	0.05	1136	6.1	5.460×10^3	Sanriku, Japan
1973	0.20	833	8.2	1.934×10^4	Sanriku, Japan
1976	0.40	1526	4.0	7.084×10^4	Palestine, USA
1977	0.63	1760	4.5	1.2772×10^5	Palestine, USA
1979	0.80	1680	4.9	1.5389×10^5	Palestine, USA
1980	0.80	2029	7.8	1.8838×10^5	Palestine, USA
1984	0.076	576	9.2	5.330×10^3	Sanriku, Japan
1985	0.087	940	9.4	9.930×10^3	Sanriku, Japan
1988	0.038	647	7.1	2.948×10^3	Uchinoura, Japan
1996	0.20	2092	4.6	4.874×10^4	Sanriku, Japan
1998	0.20	1178	5.6	2.729×10^4	Sanriku, Japan
1999	0.20	891	5.6	2.005×10^4	Sanriku, Japan
2001	0.20	1108	5.5	2.494×10^4	Sanriku, Japan

* Effective $S\Omega_e T$ for primary electron observations in the energy range above 1 TeV within the zenith angle of 60°.

Table 2. The number of the observed electrons and the fluxes of primary cosmic-ray electrons

Energy (GeV)	\bar{E} (GeV)	$S\Omega_e T$ (m ² s sr)	N_{ob}	N_{sec}	N_{pri}	Flux (J) (m ⁻² s ⁻¹ sr ⁻¹ GeV ⁻¹)	$E^3 \times J$ (GeV ² m ⁻² s ⁻¹ sr ⁻¹)
30–50	3.82×10^1	69.8	6	0	6	$(3.94 \pm 1.61) \times 10^{-3}$	220±90
60–100	7.64×10^1	682	9	0	9	$(3.15 \pm 1.05) \times 10^{-4}$	141±47
100–150	1.21×10^2	1.679×10^3	8	1.00	7.00	$(8.08 \pm 3.31) \times 10^{-5}$	143±59
150–200	1.72×10^2	5.613×10^3	7	1.43	5.57	$(1.92 \pm 0.93) \times 10^{-5}$	98±47
200–300	2.43×10^2	9.718×10^3	7	1.96	5.04	$(5.03 \pm 2.71) \times 10^{-6}$	72±39
300–400	3.45×10^2	4.8368×10^4	15	4.37	10.63	$(2.14 \pm 0.80) \times 10^{-6}$	88±33
400–600	4.86×10^2	1.3374×10^5	35	6.44	28.56	$(1.05 \pm 0.22) \times 10^{-6}$	120±25
600–800	6.90×10^2	3.2148×10^5	29	7.16	21.84	$(3.35 \pm 0.85) \times 10^{-7}$	110±28
800–1000	8.92×10^2	5.9088×10^5	20	6.54	13.46	$(1.13 \pm 0.39) \times 10^{-7}$	80±27
1000–1500	1.214×10^3	7.0795×10^5	15	7.73	7.27	$(2.03 \pm 1.14) \times 10^{-8}$	36±20
1500–3000	2.068×10^3	7.0795×10^5	15	5.31	9.69	$(9.04 \pm 3.74) \times 10^{-9}$	80±33

Table A1. List of ECC

ECC	X-ray film	Area (m ²)	Edge effect	θ_0 (deg)	$S\Omega_e T$ (m ² sr s)
1968	(SN)				
		* 30–50GeV: 19.49×10 ⁻⁴	1.000	45	6.981×10 ¹
		* 60–100GeV: 235.9×10 ⁻⁴	0.807	45	6.819×10 ²
		* 100–150GeV: 235.9×10 ⁻⁴	0.807	45	6.819×10 ²
		* 150–200GeV: 235.9×10 ⁻⁴	0.807	45	6.819×10 ²
		* 200–300GeV: 467.7×10 ⁻⁴	0.764	45	1.280×10 ³
		* 300–400GeV: 467.7×10 ⁻⁴	0.764	45	1.280×10 ³
		* 400–600GeV: 467.7×10 ⁻⁴	0.764	45	1.280×10 ³
		600–800GeV: 500.0×10 ⁻⁴	0.680	60	1.826×10 ³
		800–1000GeV: 500.0×10 ⁻⁴	0.680	60	1.826×10 ³
		1000–1500GeV: 500.0×10 ⁻⁴	0.680	60	1.826×10 ³
		1500–3000GeV: 500.0×10 ⁻⁴	0.680	60	1.826×10 ³
1969	(SN)				
		30–50GeV:
		60–100GeV:
		100–150GeV:
		150–200GeV:
		* 200–300GeV: 318.3×10 ⁻⁴	0.789	45	6.321×10 ²
		* 300–400GeV: 318.3×10 ⁻⁴	0.789	45	6.321×10 ²
		* 400–600GeV: 318.3×10 ⁻⁴	0.789	45	6.321×10 ²
		600–800GeV: 500.0×10 ⁻⁴	0.680	60	1.283×10 ³
		800–1000GeV: 500.0×10 ⁻⁴	0.680	60	1.283×10 ³
		1000–1500GeV: 500.0×10 ⁻⁴	0.680	60	1.283×10 ³
		1500–3000GeV: 500.0×10 ⁻⁴	0.680	60	1.283×10 ³
1970	(SN)				
		30–50GeV:
		60–100GeV:
		100–150GeV:
		150–200GeV:
		* 200–300GeV: 115.9×10 ⁻⁴	0.870	45	1.080×10 ³
		* 300–400GeV: 115.9×10 ⁻⁴	0.870	45	1.080×10 ³
		* 400–600GeV: 115.9×10 ⁻⁴	0.870	45	1.080×10 ³
		600–800GeV: 500.0×10 ⁻⁴	0.680	60	5.460×10 ³
		800–1000GeV: 500.0×10 ⁻⁴	0.680	60	5.460×10 ³
		1000–1500GeV: 500.0×10 ⁻⁴	0.680	60	5.460×10 ³
		1500–3000GeV: 500.0×10 ⁻⁴	0.680	60	5.460×10 ³
1973	(SN)				

Table A1—Continued

ECC	X-ray film	Area (m ²)	Edge effect	θ_0 (deg)	$S\Omega_e T$ (m ² sr s)
		30–50GeV:
		60–100GeV:
		* 100–150GeV: 127.0×10^{-4}	1.000	45	9.972×10^2
		* 150–200GeV: 127.0×10^{-4}	1.000	45	9.972×10^2
		* 200–300GeV: 407.3×10^{-4}	0.873	45	2.792×10^3
		* 300–400GeV: 407.3×10^{-4}	0.873	45	2.792×10^3
		* 400–600GeV: 407.3×10^{-4}	0.873	45	2.792×10^3
		600–800GeV: 0.20	0.821	60	1.9335×10^4
		800–1000GeV: 0.20	0.821	60	1.9335×10^4
		1000–1500GeV: 0.20	0.821	60	1.9335×10^4
		1500–3000GeV: 0.20	0.821	60	1.9335×10^4
1976	(SN)	30–50GeV:
		60–100GeV:
		100–150GeV:
		150–200GeV:
		200–300GeV:
		300–400GeV:
		400–600GeV:
		600–800GeV: 0.20	0.821	60	3.5420×10^4
		800–1000GeV: 0.40	0.821	60	7.0841×10^4
		1000–1500GeV: 0.40	0.821	60	7.0841×10^4
		1500–3000GeV: 0.40	0.821	60	7.0841×10^4
1977	(SN)	30–50GeV:
		60–100GeV:
		100–150GeV:
		150–200GeV:
		200–300GeV:
		300–400GeV:
		400–600GeV:
		600–800GeV: 0.04875	0.810	60	9.824×10^3
		800–1000GeV: 0.24375	0.810	60	4.9121×10^4
		1000–1500GeV: 0.63375	0.810	60	1.2772×10^5
		1500–3000GeV: 0.63375	0.810	60	1.2772×10^5
1979	(SN)	30–50GeV:

Table A1—Continued

ECC	X-ray film	Area (m ²)	Edge effect	θ_0 (deg)	$S\Omega_e T$ (m ² sr s)
		60–100GeV:
		100–150GeV:
		150–200GeV:
		200–300GeV:
		300–400GeV:
		400–600GeV:
		600–800GeV: 0.20	0.810	60	3.8473×10^4
		800–1000GeV: 0.60	0.810	60	1.1542×10^5
		1000–1500GeV: 0.80	0.810	60	1.5389×10^5
		1500–3000GeV: 0.80	0.810	60	1.5389×10^5
1980	(SN)	30–50GeV:
		60–100GeV:
		100–150GeV:
		150–200GeV:
		200–300GeV:
		300–400GeV:
		400–600GeV:
		600–800GeV: 0.30	0.821	60	7.0644×10^4
		800–1000GeV: 0.80	0.821	60	1.8838×10^5
		1000–1500GeV: 0.80	0.821	60	1.8838×10^5
		1500–3000GeV: 0.80	0.821	60	1.8838×10^5
1984	(SN), (G8)	30–50GeV:
		60–100GeV:
		100–150GeV:
		150–200GeV:
		200–300GeV:
		300–400GeV: 381.0×10^{-4}	0.859	60	2.665×10^3
		400–600GeV: 762.0×10^{-4}	0.859	60	5.330×10^3
		600–800GeV: 762.0×10^{-4}	0.859	60	5.330×10^3
		800–1000GeV: 762.0×10^{-4}	0.859	60	5.330×10^3
		1000–1500GeV: 762.0×10^{-4}	0.859	60	5.330×10^3
		1500–3000GeV: 762.0×10^{-4}	0.859	60	5.330×10^3
1985	(F), (G8)	30–50GeV:
		60–100GeV:

Table A1—Continued

ECC	X-ray film	Area (m ²)	Edge effect	θ_0 (deg)	$S\Omega_e T$ (m ² sr s)
		100–150GeV:
		150–200GeV:
		200–300GeV:
		300–400GeV: 762.0×10^{-4}	0.859	60	8.698×10^3
		400–600GeV: 762.0×10^{-4}	0.859	60	8.698×10^3
		600–800GeV: 870.0×10^{-4}	0.859	60	9.930×10^3
		800–1000GeV: 870.0×10^{-4}	0.859	60	9.930×10^3
		1000–1500GeV: 870.0×10^{-4}	0.859	60	9.930×10^3
		1500–3000GeV: 870.0×10^{-4}	0.859	60	9.930×10^3
1988	(F), (G12), (GS), (G8)				
		30–50GeV:
		60–100GeV:
		100–150GeV:
		150–200GeV: 381.0×10^{-4}	0.846	60	2.948×10^3
		200–300GeV: 381.0×10^{-4}	0.846	60	2.948×10^3
		300–400GeV: 381.0×10^{-4}	0.846	60	2.948×10^3
		400–600GeV: 381.0×10^{-4}	0.846	60	2.948×10^3
		600–800GeV: 381.0×10^{-4}	0.846	60	2.948×10^3
		800–1000GeV: 381.0×10^{-4}	0.846	60	2.948×10^3
		1000–1500GeV: 381.0×10^{-4}	0.846	60	2.948×10^3
		1500–3000GeV: 381.0×10^{-4}	0.846	60	2.948×10^3
1996	(F), (H8)				
		30–50GeV:
		60–100GeV:
		100–150GeV:
		* 150–200GeV: 50.0×10^{-4}	1.000	45	9.860×10^2
		* 200–300GeV: 50.0×10^{-4}	1.000	45	9.860×10^2
		* 300–400GeV: 50.0×10^{-4}	1.000	45	9.860×10^2
		400–600GeV: 0.20	0.824	60	4.8735×10^4
		600–800GeV: 0.20	0.824	60	4.8735×10^4
		800–1000GeV: 0.20	0.824	60	4.8735×10^4
		1000–1500GeV: 0.20	0.824	60	4.8735×10^4
		1500–3000GeV: 0.20	0.824	60	4.8735×10^4
1998	(F), (H12), (H8)				
		30–50GeV:
		60–100GeV:
		100–150GeV:

Table A1—Continued

ECC	X-ray film	Area (m ²)	Edge effect	θ_0 (deg)	$S\Omega_e T$ (m ² sr s)
		150–200GeV:
		200–300GeV:
		300–400GeV: 0.20	0.819	60	2.7287×10^4
		400–600GeV: 0.20	0.819	60	2.7287×10^4
		600–800GeV: 0.20	0.819	60	2.7287×10^4
		800–1000GeV: 0.20	0.819	60	2.7287×10^4
		1000–1500GeV: 0.20	0.819	60	2.7287×10^4
		1500–3000GeV: 0.20	0.819	60	2.7287×10^4
1999	(F), (H16), (H12), (H8)				
		30–50GeV:
		60–100GeV:
		100–150GeV:
		150–200GeV:
		200–300GeV:
		300–400GeV:
		400–600GeV: 0.10	0.796	60	1.0023×10^4
		600–800GeV: 0.20	0.796	60	2.0046×10^4
		800–1000GeV: 0.20	0.796	60	2.0046×10^4
		1000–1500GeV: 0.20	0.796	60	2.0046×10^4
		1500–3000GeV: 0.20	0.796	60	2.0046×10^4
2001	(F), (H16), (H8)				
		30–50GeV:
		60–100GeV:
		100–150GeV:
		150–200GeV:
		200–300GeV:
		300–400GeV:
		400–600GeV: 0.20	0.796	60	2.4937×10^4
		600–800GeV: 0.20	0.796	60	2.4937×10^4
		800–1000GeV: 0.20	0.796	60	2.4937×10^4
		1000–1500GeV: 0.20	0.796	60	2.4937×10^4
		1500–3000GeV: 0.20	0.796	60	2.4937×10^4

Note. — * Microscope scanning. See text for details.

Note. — (SN) Sakura Type-N, (G8) G8-RX0, (F) Fuji #200, (G12) G12-RXO, (H12) HR12-HA30, (GS)

GS-RXO, (H8) HR8-HA30, (H16) HR16-HA30.

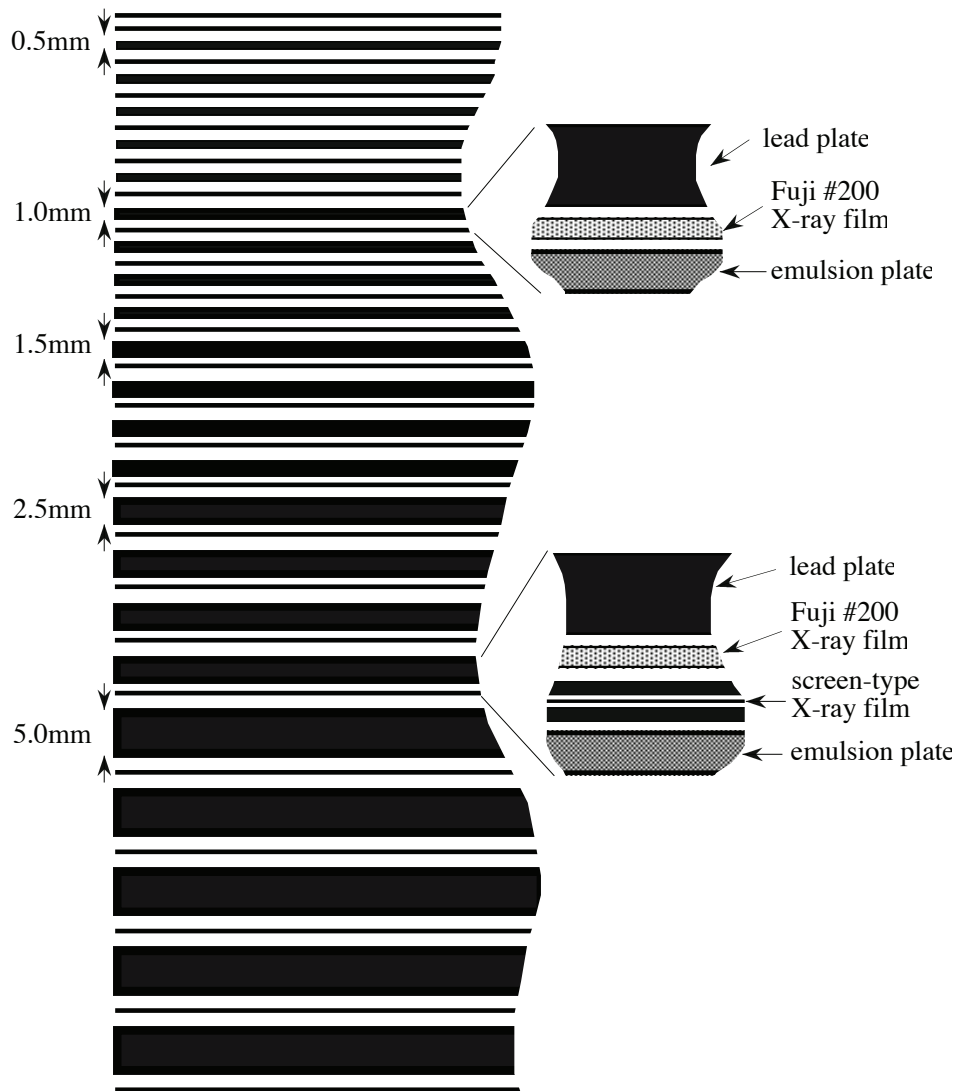


Fig. 1.— Typical configuration of the emulsion chamber in cross-sectional drawing from side view.

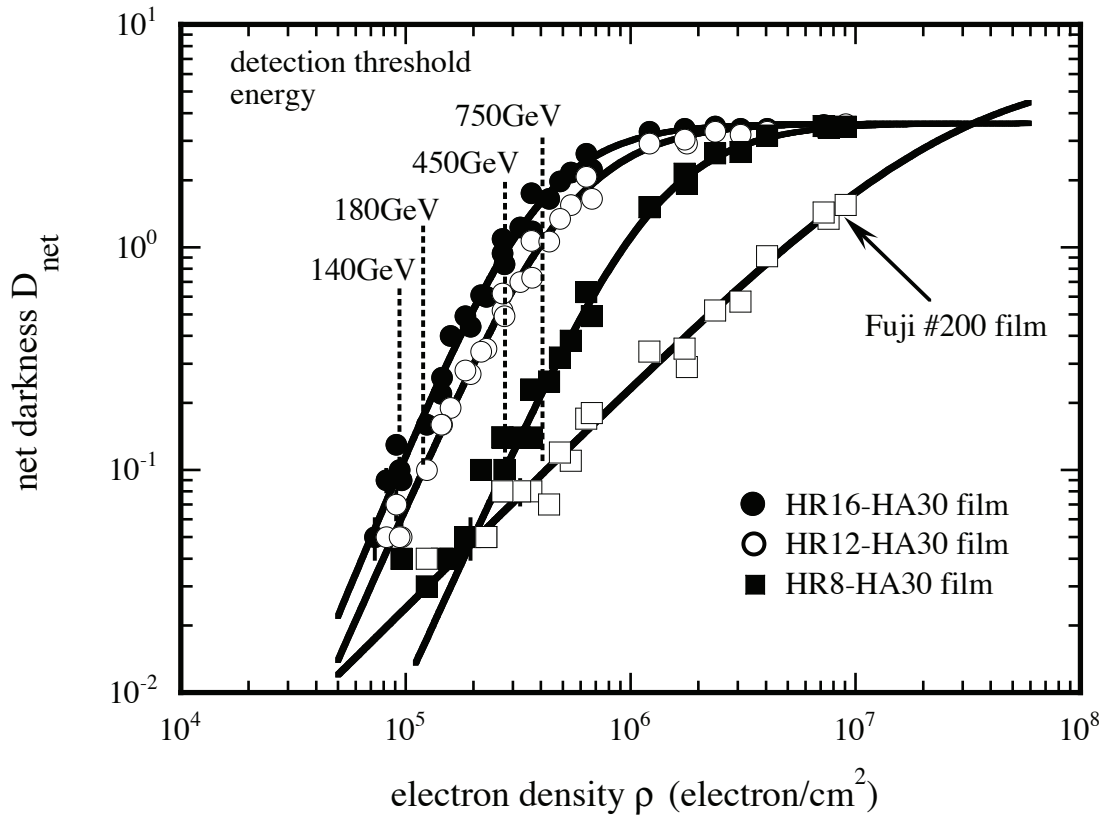


Fig. 2.— Characteristic curves for different types of X-ray films.

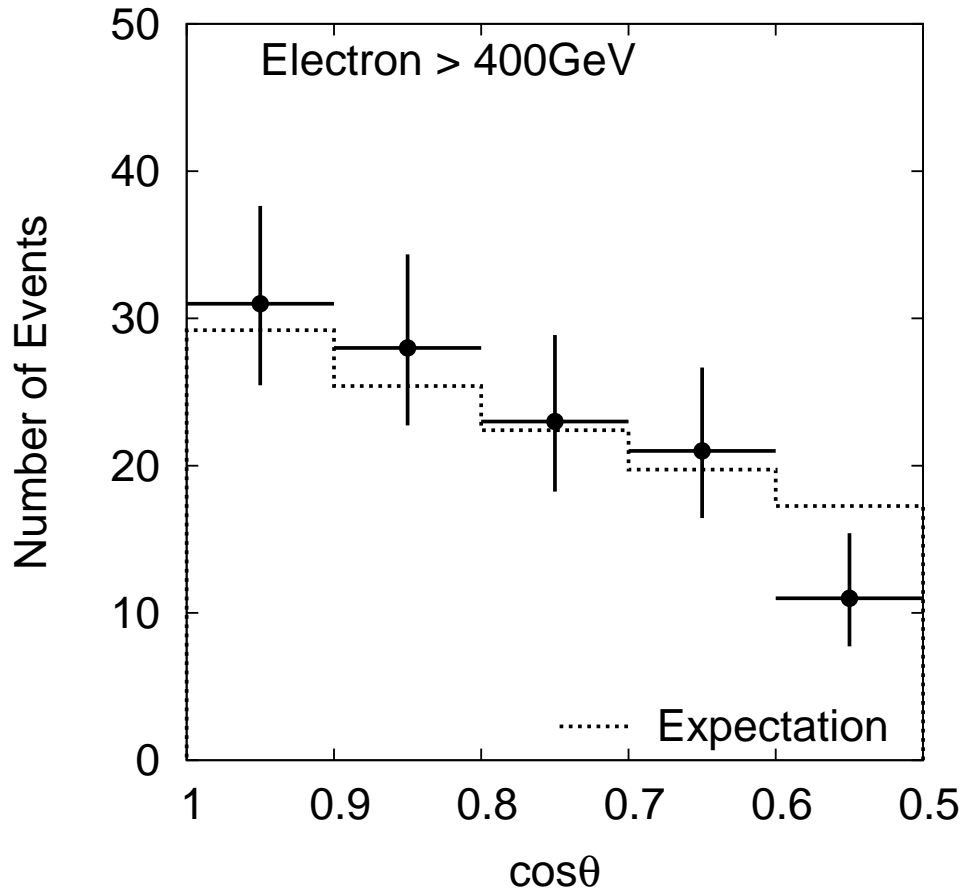


Fig. 3.— Zenith angle distributions for electrons above 400 GeV observed with the balloon-borne emulsion chambers, which is compared to the expected distribution for primary electrons.

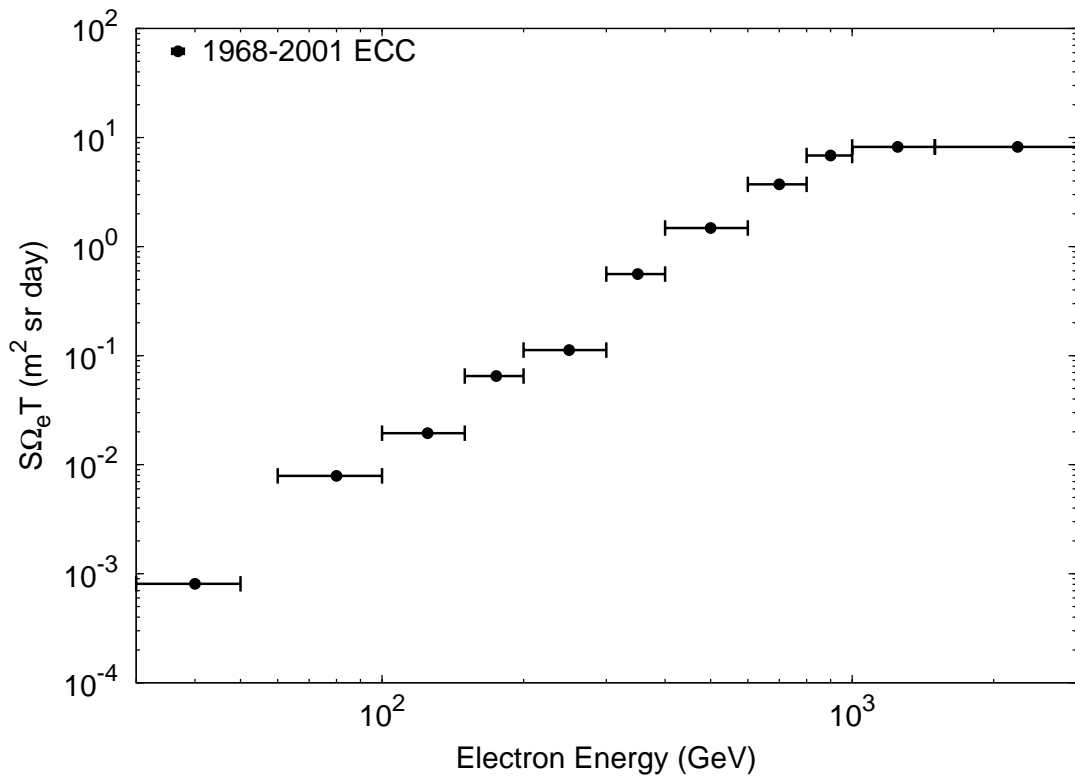


Fig. 4.— Total exposure $S\Omega_e T$ for primary electrons with electron energy.

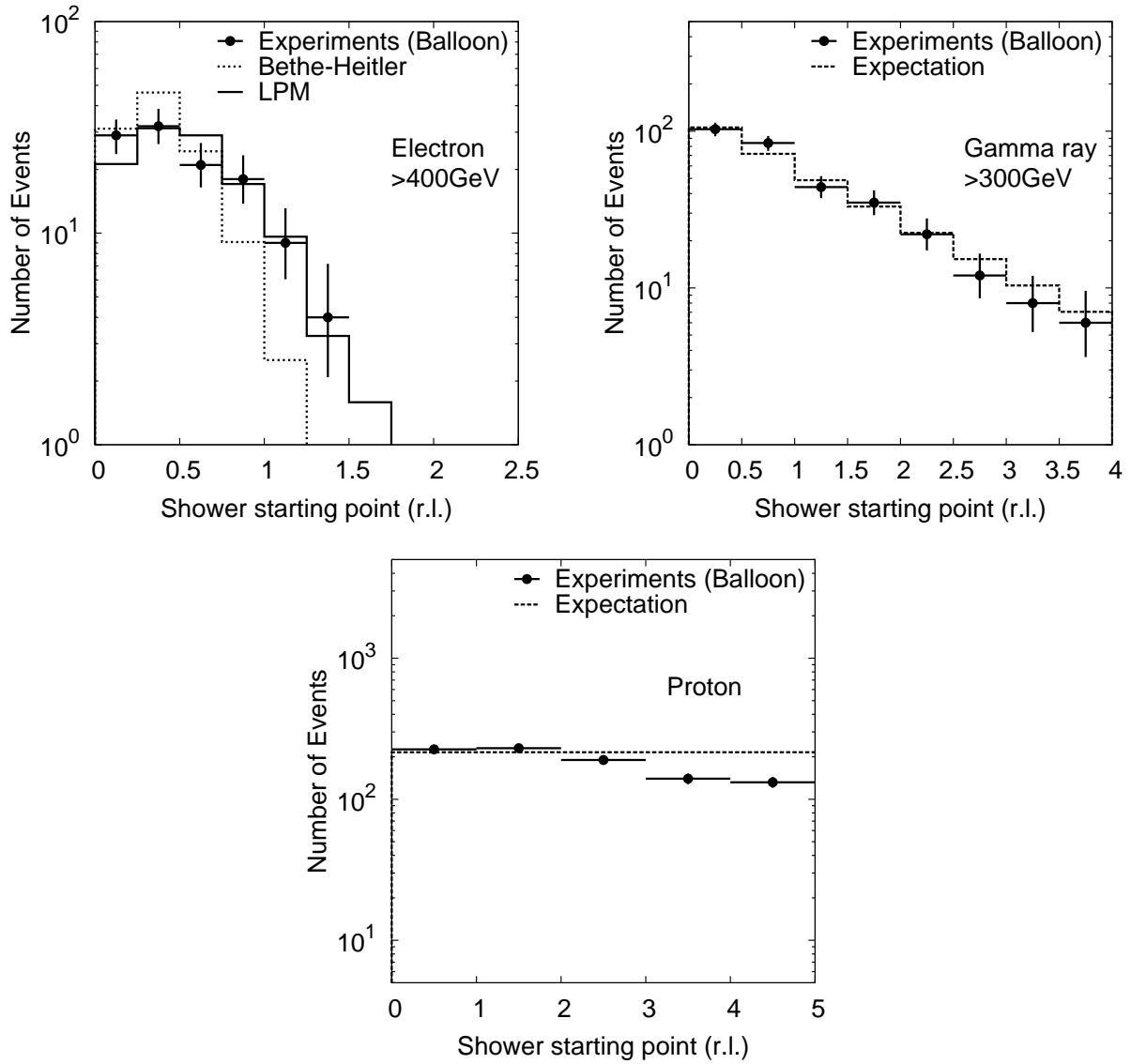


Fig. 5.— Shower starting point distributions for the observed electrons, gamma rays, and protons, compared to the expected distributions.

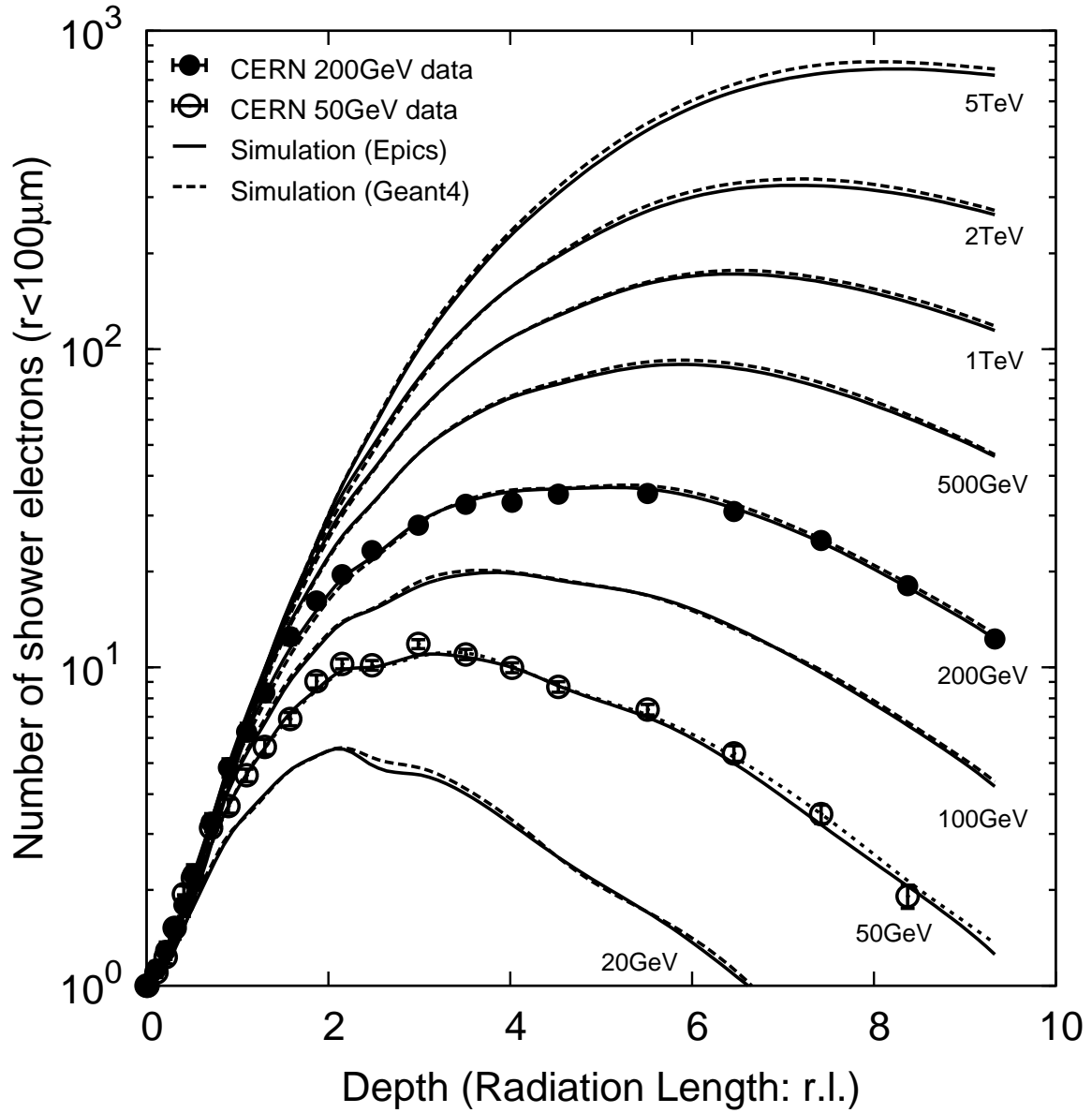


Fig. 6.— Longitudinal developments of the averaged number of shower tracks within a radius of $100 \mu\text{m}$ from the simulations, compared to the experimental data.

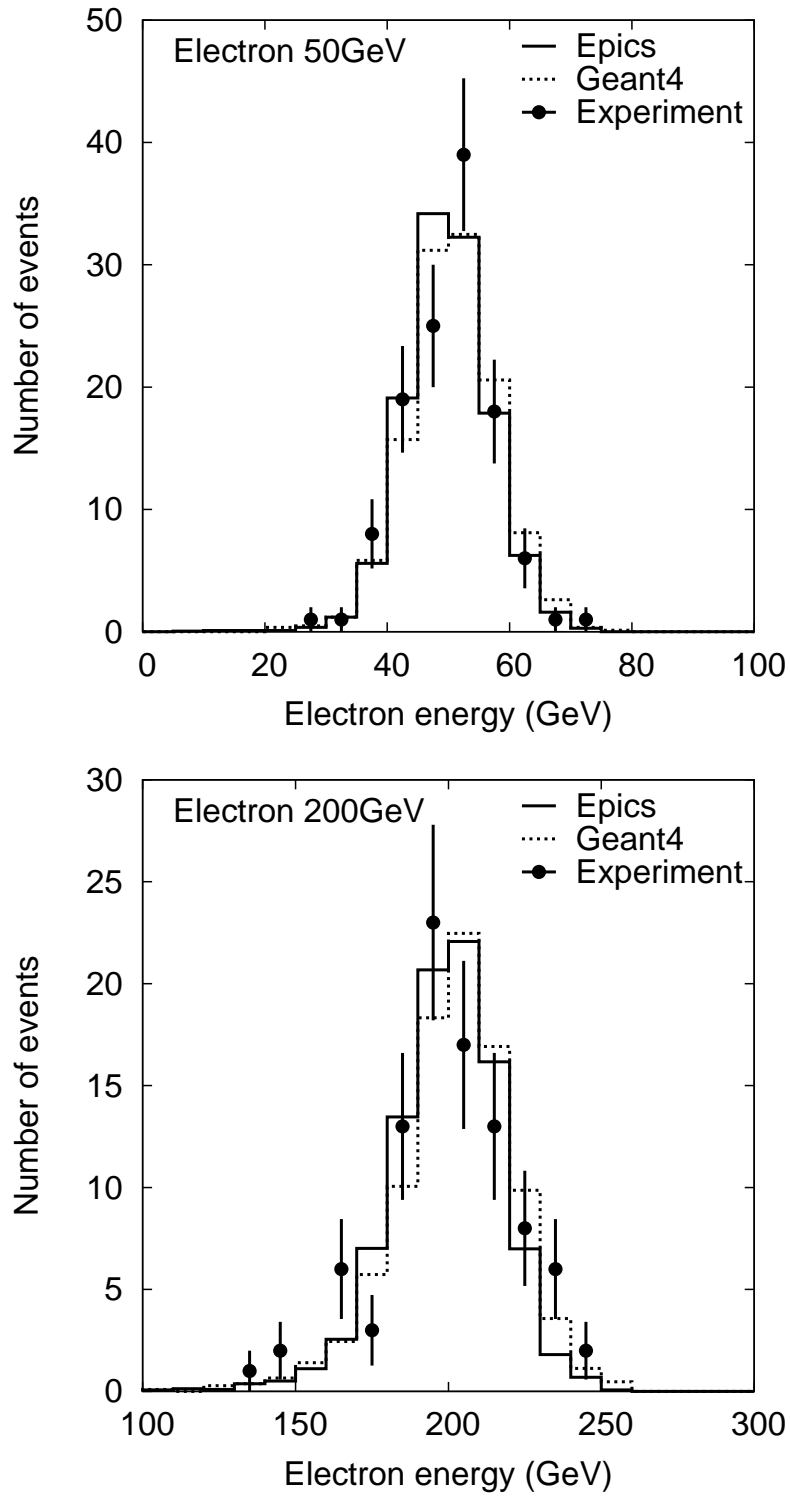


Fig. 7.— Energy distributions of the experimental data for 50 GeV and 200 GeV electron beams at CERN-SPS, compared with the simulations.

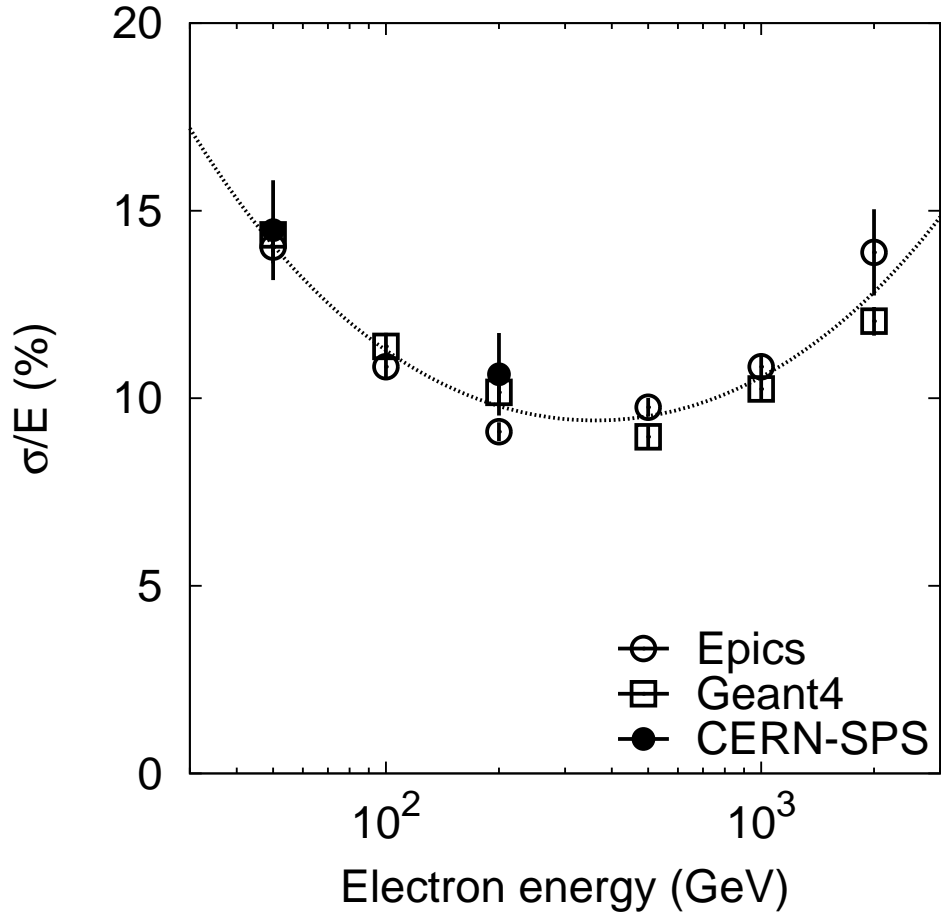


Fig. 8.— Energy dependence of energy resolutions with the emulsion chambers from the simulations, compared to the experimental data for electrons of 50 GeV and 200 GeV.

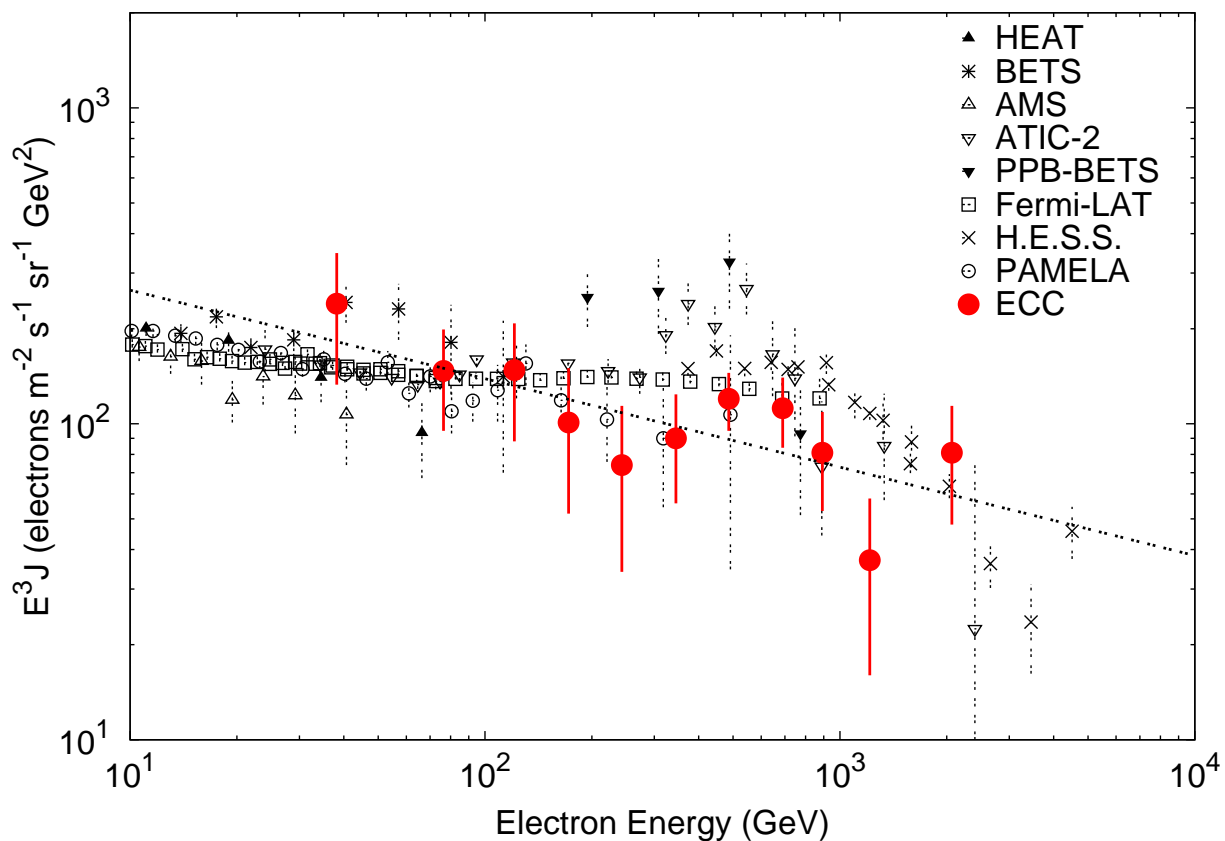


Fig. 9.— The primary cosmic-ray electron spectrum observed with the emulsion chambers (ECC), compared to the recent experiments (DuVernois et al. 2001; Torii et al. 2001; Aguilar et al. 2002; Chang et al. 2008; Ackermann et al. 2010b; Aharonian et al. 2009; Adriani et al. 2011a). The dotted line shows the best fitted power-law spectrum with an index of -3.28 .

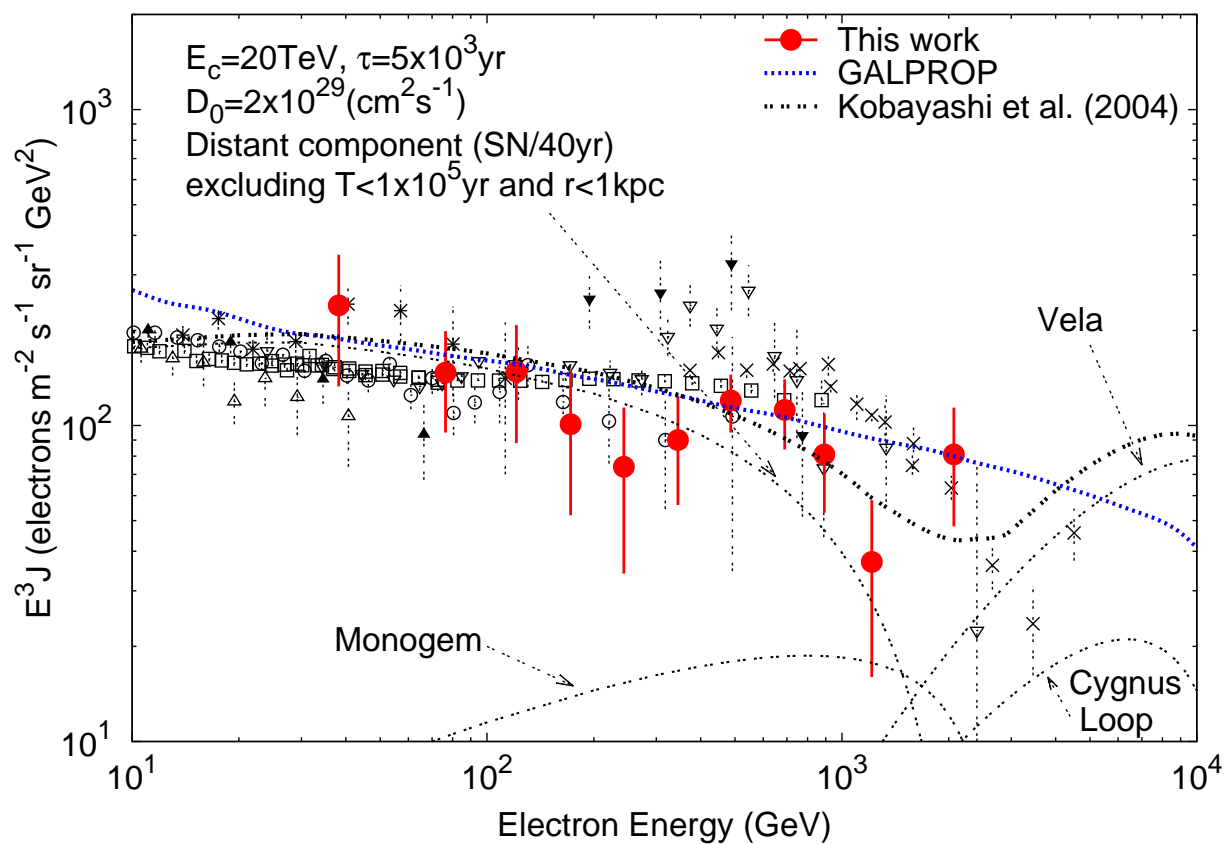


Fig. 10.— The observed electron spectrum with the emulsion chambers compared to model electron spectra, a GALPROP model with parameters of galdef_50p_599278 file and a SNRs model (a distant component + nearby components) by Kobayashi et al. (2004). See text for details.